Magnetic and ferroelectric properties of multiferroic RMn_2O_5

2008 J. Phys.: Condens. Matter 20 434206

(http://iopscience.iop.org/0953-8984/20/43/434206)

J. Phys.: Condens. Matter **20** (2008) 434206 (13pp) doi:10.1088/0953-8984/20/43/434206

Magnetic and ferroelectric properties of multiferroic RMn_2O_5

Y Noda[1], H Kimura[1], M Fukunaga[1], S Kobayashi[2], I Kagomiya[3] and K Kohn[4]

[1] Institute of Multidisciplinary Research for Advanced Materials, Tohoku University 2-1-1 Katahira, Aoba-ku, Sendai 980-8577, Japan
[2] Non Destructive Evaluation and Science Research Center, Faculty of Engineering, Iwate University, Morioka 020-8551, Japan
[3] Material Science and Engineering, Nagoya Institute of Technology, Nagoya 466-8555, Japan
[4] Department of Physics, Waseda University, Tokyo 169-8555, Japan

E-mail: ynoda@tagen.tohoku.ac.jp

Received 21 April 2008, in final form 8 July 2008
Published 9 October 2008
Online at stacks.iop.org/JPhysCM/20/434206

Abstract

The magnetic and ferroelectric properties of multiferroic RMn_2O_5 (R = Y, Tb, Ho, Er, Tm) are reviewed based on recent neutron diffraction and dielectric measurements. Successive phase transitions of magnetic and dielectric ordering were found to occur simultaneously in this system. The characteristic magnetic ordering of the system exhibits an incommensurate–commensurate phase transition, and again transitions to an incommensurate phase. Special attention is given to the magnetic structure in order to discuss the mechanism for the introduction of ferroelectric polarization. For all the compounds examined, the spin configuration for Mn^{4+} and Mn^{3+} ions in the commensurate magnetic phase, where spontaneous electric polarization occurs, was determined to be a transverse spiral spin structure propagating along the *c*-axis. By contrast, the alignment of the induced 4f moment of R^{3+} ions showed variation, depending on the character of each of the elements. Corresponding responses to external fields such as a magnetic field, hydrostatic pressure etc at low temperature are strongly dependent on the rare earth element present in the RMn_2O_5 system. The so-called colossal magnetoelectric effect in this system can be easily interpreted by the phase transition from the magnetic incommensurate and weak ferroelectric phase to the commensurate and ferroelectric phase.

(Some figures in this article are in colour only in the electronic version)

1. Introduction

'Multiferroics', in which the (anti)ferromagnetic (AFM or FM) and ferroelectric (FE) orders coexist and are mutually coupled, is a recent hot topic in solid state physics. The terminology 'ferroic' and 'prototype' was first used by Aizu [1] to simultaneously discuss the symmetry of ferroelectric, ferromagnetic and ferroelastic properties. However, the simultaneous existence of different ferroic orders is very rare and was not found for a long time, except for a few examples such as perovskite type compounds ABO_3 with magnetically active elements [2], the hexagonal ABO_3 group and the $BaMX_4$ material group. An example of an extensively studied system is $BiFeO_3$ [3] (T_N = 643 K and T_c > 1100 K). A thorough review of work in this field has already been made by Fiebig [4]. Cross-correlation of the magnetoelectric (ME) effect, such as the effect on dielectric properties by application of a magnetic field, has been long investigated; however, the effect is so small as to preclude its use in an application field.

Recent discoveries of the colossal ME effect in rare earth manganites of $TbMnO_3$ by Kimura *et al* [5], *hex*-$ErMnO_3$ by Iwata *et al* [6], $YbMn_2O_5$ by Koyata *et al* [7], $ErMn_2O_5$ by Koyata *et al* [8], $TmMn_2O_5$ by Iwata *et al* and Uga *et al* [9, 10], YMn_2O_5 by Popov *et al* [11], $TbMn_2O_5$ and $DyMn_2O_5$ by Hur *et al* [12, 13] have provided a new and different perspective in this field. They discovered that the electric polarization can be induced, flipped and flopped by the influence of an external magnetic field. Thus, the ferroelectric state can be controlled, not only by an external electric field,

but also using a magnetic field. The case of $TbMnO_3$ is even more fascinating. Polarization flop by magnetic field and polarization flip by electrical field provides four states of the system. This four-state system can be applied as a memory device by using only one material, and this will presumably open a new era for application.

In this paper, we will present recent progress in the studies of the magnetic and ferroelectric properties of multiferroic RMn_2O_5 (R = Y, Tb, Ho, Er, Tm) compounds, with emphasis on the variety of materials by change in the rare earth element composition. The ferroelectric properties and ME effect of RMn_2O_5 were studied by Sanina *et al* [14, 15] for R = Eu and also extensively by Kohn's group in the 1990s [7–10, 16–20] (see also their review paper [21]). At the early stage of their studies, there was some confusion on the phase transition temperatures, partially because of the sample dependence and different measurement probes, and also because the transition scheme was very complicated. The transition scheme has since been fully understood, and is described in detail in this paper.

The crystal structures of RMn_2O_5 (R = rare earth, Bi, and Y) were first well established by Bertaut *et al* [22] and independently by Abrahams and Bernstein [23] and then later by many authors [24–32]. It is orthorhombic at room temperature with the $Pbam$ space group ($Z = 4$). It contains edge-shared $Mn^{4+}O_6$ octahedra connecting along the c-axis, and pairs of $Mn^{3+}O_5$ pyramids linking with two $Mn^{4+}O_6$ chains. The Mn^{4+}, Mn^{3+}, and rare earth R^{3+} ions have magnetic moments, which are responsible for the complex magnetism. Figure 1 shows the crystal structure of RMn_2O_5 projected on the ab- and bc-planes. The typical unit cell size of RMn_2O_5, for R = Y as an example, is $a = 7.28, b = 8.50$ and $c = 5.69$ Å. There are five magnetic interactions between neighboring spins through the Mn^{4+}–Mn^{4+} path, and the Mn^{3+}–O–Mn^{4+}, Mn^{3+}–O–Mn^{3+}, and Mn^{4+}–O–Mn^{4+} bonds, as shown in figure 1. Such a complicated interaction scheme was already identified by Abrahams and Bernstein [23] in their crystal structure analysis report. The notation used for interaction J in figure 1 follows [25, 26]. If R^{3+} ions are magnetically active, additional interactions must be considered. Thus, these competing interactions make the system highly frustrated, yielding various magnetically ordered phases with long modulation wavelengths, as mentioned later.

The magnetic structure of RMn_2O_5 was first studied by Buisson [27, 28] using powder neutron diffraction. They had already found that the magnetic Bragg reflection could be indexed in terms of an incommensurate structure with propagation vectors $(\frac{1}{2}, 0, q_z)$. Later, Wilkinson *et al* [29, 30] reinvestigated $DyMn_2O_5$ using single crystal neutron diffraction, and found that the propagation vector was $(q_x, 0, q_z)$ below the magnetic phase transition temperature T_N. At very low temperature, the moment from Dy^{3+} becomes major, and the propagation vector was found at $(\frac{1}{2}, 0, q_z)$ and $(\frac{1}{2}, 0, 0)$. The magnetic structure reported is very complicated, but is essentially an antiferromagnetic arrangement expressed by a helical or sinusoidal spin structure on the ab-plane. Until 2000, there was no realization of the strong correlation between the ferroelectric and magnetic phase transitions in

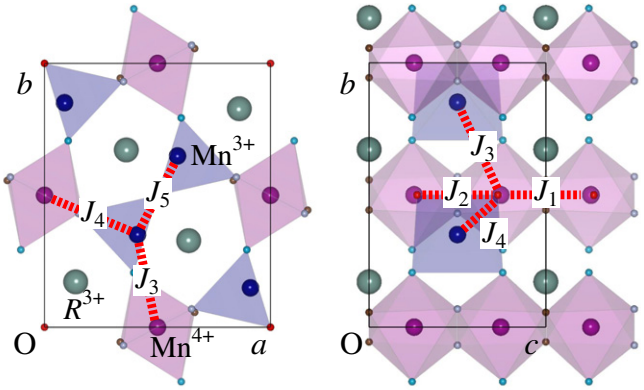

Figure 1. Crystal structure of RMn_2O_5 in the paraelectric phase, projected on the ab-plane (left panel) and bc-plane (right panel). Magnetic interaction between Mn atoms is expressed by J.

RMn_2O_5, thus the magnetic properties were solely discussed. When the magnetic structure of RMn_2O_5 was properly solved, the discovery of the coincidence of magnetic and ferroelectric phase transitions, in particular, the existence of the commensurate magnetic phase coincident with the ferroelectric phase [33], was crucially important. The magnetic structure of the commensurate phase in YMn_2O_5 was solved immediately after this discovery [34]. A model-free magnetic structure analysis is presented in detail hereafter.

After the discovery of multiferroic properties, theories to explain the electric polarization induced by magnetic moments were given. So far, two distinct scenarios have been proposed for the microscopic mechanism of magnetically induced ferroelectricity. One scenario is the spin chirality ($\mathbf{S}_i \times \mathbf{S}_j$) between noncollinearly aligned spins, typically expressed by a transverse spiral spin structure [35, 36]. Such interaction induces electric polarization, i.e. uniform atomic displacement, due to the Dzyaloshinskii–Moriya (DM) interaction [37, 38] as an inverse effect. The other scenario is the so-called 'exchange striction', given by the $\mathbf{S}_i \cdot \mathbf{S}_j$ product between neighboring spins [39, 40]. In this scenario, the atomic displacements are induced by dependence of the exchange coupling on the distance and angle, which can break the inversion symmetry in the crystal and generate electric polarization.

With regard to the origin of ferroelectricity in RMn_2O_5, Chapon *et al* proposed that the electric polarization in this material is reproducible by an $\mathbf{S}_i \cdot \mathbf{S}_j$-type interaction based on the magnetic structure obtained by powder neutron experiments [25, 26, 41], that is, in support of the latter scenario. However, we have appropriated a stance using the former scenario, based on a single crystal model-free magnetic structure analysis [31, 32, 34]. At the present stage, a definite conclusion has not yet been realized, because the relation between atomic displacement and magnetic moment is not clear. We will discuss the origin of ferroelectricity in RMn_2O_5 in detail from an experimental perspective.

2. Experimental details

Single crystals of RMn_2O_5 (R = Y, Tb, Ho, Er, Tm) were grown by the PbO–PbF_2 flux method [42]. D–E hysteresis

loops were obtained using a Sawyer–Tower circuit. The amplitude of the ac voltage applied to the sample was typically 1000 V, and the frequency was 20 Hz. The permittivity or dielectric constant ε was measured with an ac amplitude of 1.4 V and frequency ranging from 1 kHz to 1 MHz. Pyroelectric measurements on the same samples were also performed. A liquid He cryostat or 3 K He-gas closed-type refrigerator were used. The current induced by the temperature-dependent polarization was recorded during zero-electric-field cooling (ZFC) or electric-field cooling (FC), and subsequent zero-electric-field heating (ZFH). The leakage current due to the applied voltage was negligible below 50 K, and measurement during FC was possible.

Neutron diffraction measurements for crystal and magnetic structure analyses were performed using a four-circle off-center neutron diffractometer (FONDER) [43] installed at the JRR-3M reactor of the Japan Atomic Energy Agency (JAEA-JRR3). The wavelength of the incident neutron beam was fixed at $\lambda = 1.254$ Å using a Ge311 monochromator. The typical crystal size was approximately 40 mm^3. Sample temperature was controlled down to 2.5 K using a closed-cycle He-gas refrigerator. Simultaneous neutron magnetic scattering, dielectric, and polarization measurements were also performed. Measurement of the D–E loops and ε were automatically switched alternately, and performed immediately after the reciprocal lattice scan at each temperature. Neutron diffraction measurements under magnetic field were also performed using the TAS-2 thermal neutron triple-axis spectrometer installed at JAEA-JRR3. The sample was mounted on the (h 0 l) scattering plane with a vertical-field superconducting magnet, which results in an applied field perfectly along the b-axis. The incident and final energies of neutrons were fixed at 14.3 meV using a pyrolytic graphite PG002 monochromator and an analyzer. A pyrolytic graphite filter was also inserted in front of the sample to reduce higher-order contamination. The experimental collimation configuration was 15′–80′–80′–80′. For the field cooling process, the magnetic field was applied at 60 K, far above T_N.

Neutron diffraction measurements under hydrostatic-pressure were performed using the thermal neutron triple-axis spectrometer (AKANE) installed at JAEA-JRR3. The sample was installed in a clamp type pressure cell and mounted on the (h 0 l) scattering plane. The incident energy of neutrons was fixed at 19.5 meV using a Ge311 monochromator.

Synchrotron radiation x-ray (SR) experiments were performed at the Photon Factory (PF) BL4C and BL1B beam lines of the High Energy Accelerator Research Organization (KEK). A four-circle diffractometer with a closed-cycle-type He-gas refrigerator was used. The x-ray wavelength used was 0.738 Å. Samples of YMn_2O_5 and $TbMn_2O_5$ with crystal dimension of approximately 200 μm were used. Precise SR experiments were also performed at BL02B1 of SPring-8, using high energy x-rays, 0.3815 Å.

3. Simultaneous and successive phase transitions

The phase transition scheme of YMn_2O_5 is shown in the left-hand panel of figure 2 for several physical properties as a function of temperature. Since the Y atom has no magnetic moment, it is the simplest case among the RMn_2O_5 family. Magnetic susceptibility, dielectric constant and electric polarization are shown in the figure. A magnetic phase transition occurs at $T_N = 45$ K, and the magnetic susceptibility along the a-axis decreases below T_N. This implies that the fluctuation of the a-component in the magnetic moment becomes ordered at T_N. Just 5 K below T_N, the dielectric constant ε along the b-axis shows a peak at $T_{C1} = 40$ K, and the electric polarization along the b-axis increases. Kohn *et al* [21] emphasized that the 5 K difference between the magnetic and ferroelectric phase transitions is extraordinarily small compared with other existing multiferroic compounds such as $BiFeO_3$. At T_{C1}, almost no anomaly is observed for the magnetic susceptibility shown in the upper panel of the figure. On further cooling, an additional phase transition occurs at T_{C2}, and peculiar behavior is observed in the spontaneous polarization, which decreases and almost disappears at T_{C2}, or rather it displays a polarization flip to the negative b-axis. This behavior implies characteristics of the so-called ferrielectric moments or two-sublattice systems well known among ferroelectric researchers. At T_{C2}, the magnetic susceptibility exhibits a stepwise anomaly, and the dielectric constant shows a sudden increase. Or at least, the fluctuation of the electric polarization along the b-axis increases below T_{C2}. In the right-hand panel of the figure, the data of the dielectric constant of R = Er, Tm and Ho are shown as a function of temperature. As clearly shown, the behavior around 40 K is very similar for these compounds, but the behavior in the lower temperature region is obviously dependent on the rare earth elements.

Let us explain the terminology ‘ferroelectricity’ briefly here. From the historical viewpoint, Rochelle salt (RS) is the well known first discovered ferroelectric compound [44]. Spontaneous polarization of RS was found between 255 and 297 K, but the behavior of the polarization was very peculiar as a function of temperature. Later, this peculiar behavior was completely understood using the two-sublattice model [45]. That is, two independent order parameters compete with each other so that the total polarization behaves like ferrimagnetic properties. Thus, such a system or material is called a ferrielectric compound in general by analogy with magnetic compounds. The similarity is also seen in ferroelastic and ferrielastic compounds [46, 47].

Neutron magnetic scattering measurements were performed using a single crystal to determine the magnetic structure. The first sample that was examined was YMn_2O_5 [33, 34, 48]. Below the magnetic phase transition temperature T_N, magnetic superlattice reflections were found, which are indexed as (q_x, 0, q_z). That is, the magnetic propagation vector $\mathbf{q}_M$ is a two-dimensionally modulated vector. Let us call this magnetic phase a two-dimensionally modulated incommensurate magnetic phase (2DICM). This result is consistent with that previously reported [29], as mentioned in the previous section. The indices q_x and q_z are expressed as $q_x = \frac{1}{2} + \delta_x$ and $q_z = \frac{1}{4} + \delta_z$.

When the temperature decreases, the modulation vector $\mathbf{q}_M$ changes as a function of temperature. Finally, $\mathbf{q}_M$ locks into

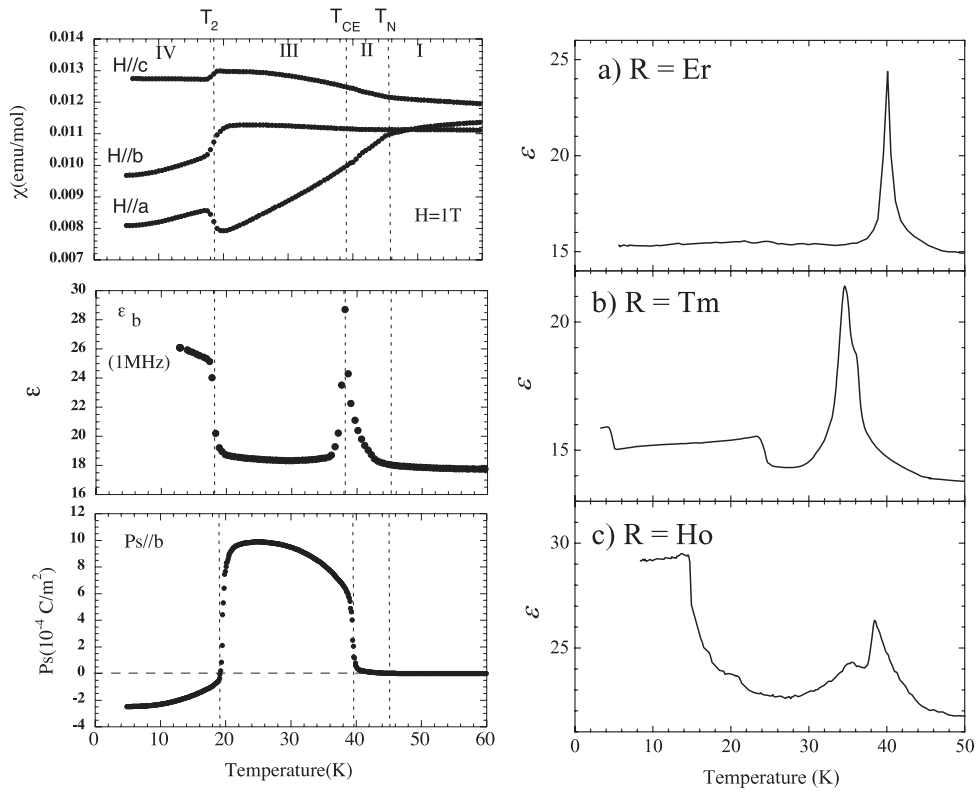

Figure 2. Magnetic susceptibility (top left), dielectric constant along the *b*-axis (middle left), and spontaneous polarization along the *b*-axis (bottom left) of YMn_2O_5. The figure is taken from [34]. The notation of the phase transition temperature is slightly different from this paper. Hereafter, T_{C1} and T_{C2} are used instead of T_{CE} and T_2. The right-hand panel shows the dielectric constant of R = Er, Tm and Ho as a function of temperature.

a commensurate phase, indexed as $\mathbf{q}_M = (\frac{1}{2}, 0, \frac{1}{4})$ [33, 48]. That is, the system changes into the commensurate magnetic phase (CM). This is the first observation of the 2DICM to CM phase transition for the RMn_2O_5 system. Let us call the magnetic phase transition temperature T_{CM}, of which an anomaly is not seen in the magnetic susceptibility measurements shown in the left-upper panel of figure 2. It is interesting to note that the magnetic and ferroelectric transition temperatures are exactly the same ($T_{CM} = T_{C1}$). Just around T_{CM} and T_{C1}, $\mathbf{q}_M$ and the dielectric constant exhibit very complicated behavior, and this is discussed later. When the temperature decreases further, $\mathbf{q}_M$ changes again to the incommensurate phase, indexed as $\mathbf{q}_M = (q_x, 0, q_z)$ at T_{ICM}, or simply T_{N2}. This low temperature two-dimensionally modulated incommensurate magnetic phase is denoted the LT-2DICM phase. Again, the magnetic and ferroelectric transition temperatures are exactly the same ($T_{ICM} = T_{C2}$). The detailed measurement of the magnetic propagation vector $\mathbf{q}_M$ in YMn_2O_5 [48] is shown as a function of temperature in the left panel of figure 3; q_x and q_z are shown separately in the figure.

Considering the complicated behavior around T_{CM} and T_{C1}, even from the old data, the dielectric constant ε of YMn_2O_5 exhibits a shoulder structure around the very sharp peak at T_{C1}, and also additional transition behavior is observed for the magnetic propagation vector $\mathbf{q}_M$. From very precise measurements, it was found that $(q_x, 0, q_z)$ first locks at T_D, 1 K above T_{CM}, to $(q_x, 0, \frac{1}{4})$,and then locks at $(\frac{1}{2}, 0, \frac{1}{4})$, as shown in figure 3. Thus, this narrow intermediate phase is denoted a one-dimensionally modulated incommensurate magnetic phase (1DICM).

The second example is $ErMn_2O_5$. The behavior of the magnetic propagation vector $\mathbf{q}_M$ for $ErMn_2O_5$ [49, 50] is almost the same as that for YMn_2O_5, and is shown in the middle panel of figure 3. The only difference is that the magnetic propagation vector $\mathbf{q}_M$ below T_{ICM} or T_{N2} indicates a one-dimensionally modulated incommensurate phase indexed as $(\frac{1}{2}, 0, q_z)$. Thus, the lowest temperature phase of $ErMn_2O_5$ is referred to as LT-1DICM, and it is different to the 1DICM phase of higher temperature, indexed as $(q_x, 0, \frac{1}{4})$. In addition, relatively strong higher harmonics $3\mathbf{q}_M$ of magnetic superlattice reflections were found in the LT-1DICM phase of $ErMn_2O_5$. This is in contrast to the LT-2DICM phase of YMn_2O_5.

The third example is $TmMn_2O_5$ [51, 52]. The behavior of the magnetic propagation vector $\mathbf{q}_M$ down to the LT-2DICM phase is again essentially the same as that of YMn_2O_5, but an additional phase transition occurs at T_{N3}, as shown in the right panel of figure 3. The anomaly of the dielectric constant at T_{N3} is also seen in figure 2. The phase transition at T_{N3} is somewhat unusual. These two phases are referred to as LT-2DICM, and LT-2DICM′ from the higher temperature phase. The magnetic propagation vector $\mathbf{q}_M$ indicates both as incommensurate phases, and also the wavevector is almost

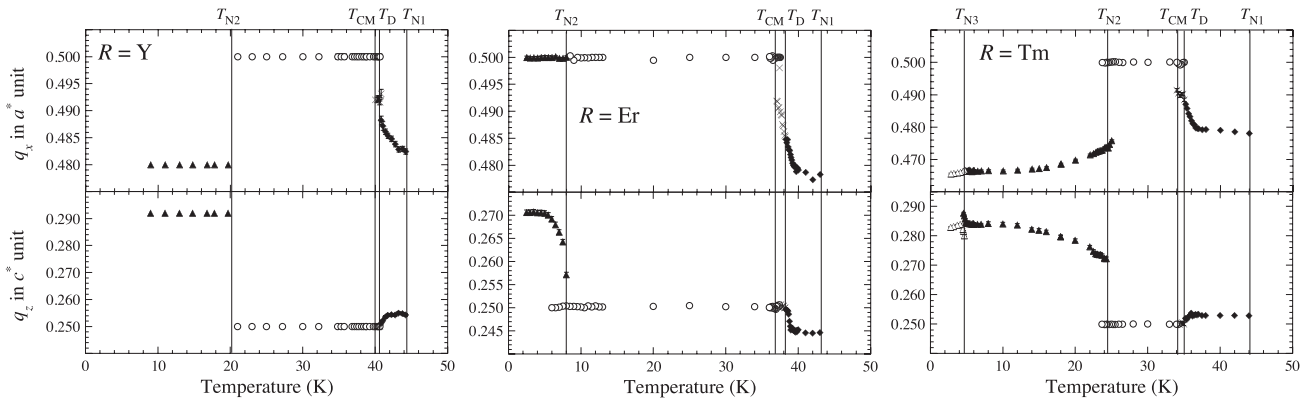

Figure 3. Magnetic propagation vectors for RMn_2O_5 (R = Y, Er and Tm). Each of the components, q_x and q_z, are separately shown for each compound.

the same, except just around the transition temperature T_{N3}. However, it is definitely considered that T_{N3} is the magnetic phase transition temperature, because the magnetic Bragg intensity pattern changes at this temperature. Thus, the magnetic moment pattern changes with the same wavevector. Later, this LT-2DICM′ phase is discussed in connection with the polarization flop transition.

Similar experiments were performed on other RMn_2O_5 compounds, R = Ho [53] and R = Tb [54]. The behavior of the magnetic propagation vector $\mathbf{q}_M$ for these two compounds is again the same as that of YMn_2O_5 down to the LT-2DICM phase. Thus, it was considered that the basic magnetic structure, and also the origin of the phase transition of the CM phase, is essentially the same among RMn_2O_5 regardless of the R^{3+} ion. In contrast, the variety of magnetic and dielectric behavior below T_{C2} originates from the character of the R^{3+} ions.

Now, let us discuss the dielectric properties of RMn_2O_5 in more detail. Data for YMn_2O_5 are already shown in figure 2. Kobayashi *et al* systematically reinvestigated the dielectric constant of RMn_2O_5 (R = Y, Tb, Tm, Er and Bi) using the same samples cut from those used for neutron diffraction measurements [55]. They summarized the dielectric and magnetic phase diagram, and pointed out the general character of the phase transition scheme for RMn_2O_5. Very recently, Fukunaga *et al* started the simultaneous measurement of the magnetic propagation wavevector, electric polarization and dielectric constant for $ErMn_2O_5$ [50] and $TmMn_2O_5$ [52] in order to determine the exact relation of the magnetic and dielectric phase transition temperatures. In addition, they made a very detailed investigation of the nature of the polarization. Data for $ErMn_2O_5$ are shown in figure 4. If the ferroelectric phase transition temperature is defined as the peak of the dielectric constant ε, it is clearly determined as T_{C1} from figure 4(e). In the usual case, spontaneous polarization appears immediately below the ferroelectric phase transition temperature. However, as seen in figure 4(d), spontaneous polarization of $ErMn_2O_5$ gradually increases from T_D, and steeply increases below T_{C1}. Thus, the narrow intermediate phase is characterized as a weak ferroelectric phase with 1DICM magnetic character. Such extraordinary

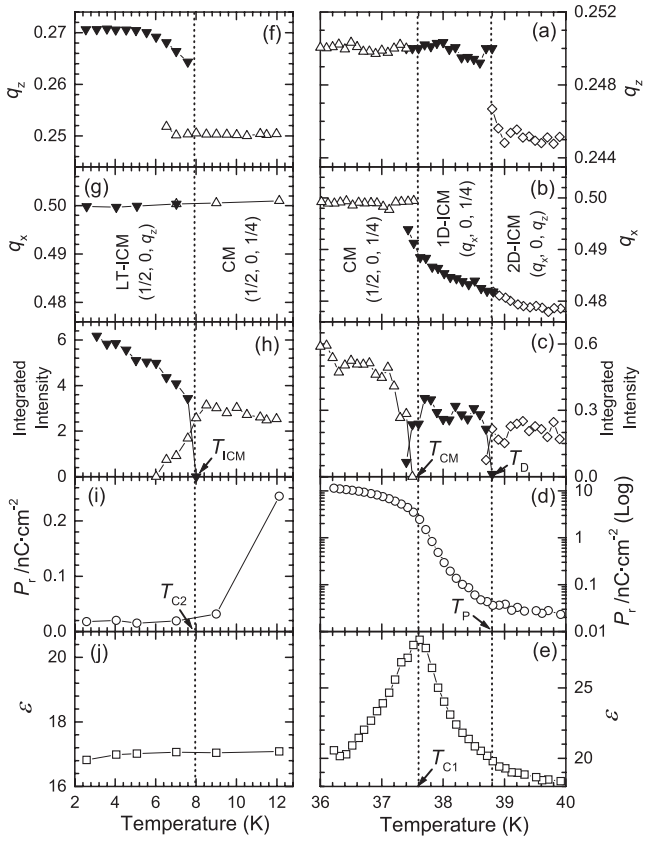

Figure 4. Results of simultaneous measurements of the propagation wavevector, integrated intensity, remanent polarization and permittivity ε of $ErMn_2O_5$ around the ferroelectric phase transition T_{C1} ((a)–(e)) and around T_{C2} ((f)–(j)), taken from [50]. The magnetic phases are labeled in (b) and (g), and the vertical dotted lines indicate the phase boundaries. The phase transition temperatures are marked in the figures.

behavior of the spontaneous polarization is reminiscent of the incommensurate–commensurate ferroelectric phase transition in $NaNO_2$.

The character below T_{C2} and T_{N2} of $ErMn_2O_5$ is slightly different from that of other RMn_2O_5 compounds. Almost no anomaly is found for the dielectric constant ε along the

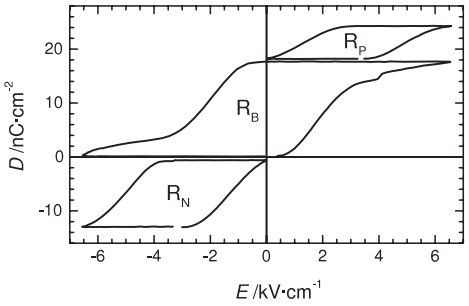

Figure 5. The ferroelectric and antiferroelectric component of the D–E hysteresis loops of $ErMn_2O_5$ taken by the newly developed method [57].

b-axis at T_{C2}. The magnetic character is LT-1DICM, and spontaneous polarization disappears, as shown in the left panel of figure 4, probably because of the high coercive field. A small polarization at 5 K was confirmed by pyroelectric measurements, and Fukunaga *et al* [50] described this lowest-temperature phase as weak ferroelectric.

$TmMn_2O_5$ is a more typical, but somewhat complicated, case [52, 55, 56]. The dielectric constant shows a stepwise anomaly at T_{C2} as for YMn_2O_5 shown in figure 2. The spontaneous polarization behavior below T_{C2} is very peculiar. As shown in figure 2, pyroelectric measurements indicate that the spontaneous polarization almost disappears or changes direction for YMn_2O_5. On the other hand, for $TmMn_2O_5$, it first vanishes and then comes back again. This behavior is very typical of ferrielectric character. Thus, the nature of the LT-2DICM phases of $TmMn_2O_5$ and YMn_2O_5 below T_{C2} seem the same.

A very exciting discovery was recently made, in which polarization flop from the b-axis to the a-axis occurred below T_{C3} and T_{N3} in $TmMn_2O_5$ [52]. This suggested the possibility of a colossal ME effect by external magnetic field, very similar to that for $TbMnO_3$ reported by Kimura *et al* [5]. In addition, our new technique for D–E hysteresis measurements recently reveals the coexistence of ferroelectric and antiferroelectric components in the ferroelectric phase of $ErMn_2O_5$ [57]. In figure 5, the observed ferroelectric and antiferroelectric components of the D–E hysteresis loops of $ErMn_2O_5$ are shown. Therefore, the ferrielectric nature of RMn_2O_5 compounds should be reinvestigated in detail.

Measurements of the D–E hysteresis loop and pyroelectric current in RMn_2O_5 are now considered. The first is a coercive electric field; at low temperature, the coercive field becomes large so that the polarization does not become saturated. In an extreme case, D–E hysteresis loops cannot be measured at all. There is another difficulty in pyroelectric current measurements of RMn_2O_5. In the ZFC case, the random distribution of ferroelectric domains is expected. In contrast, positive and negative electric-field cooling (FC) induce the opposite distribution of ferroelectric domains, and corresponding positive or negative pyroelectric currents can be observed. However, for RMn_2O_5, there is a tendency that an almost single domain or an unbalance of domain distribution is achieved at ZFC if the crystal quality is good with regard to the diffraction [56].

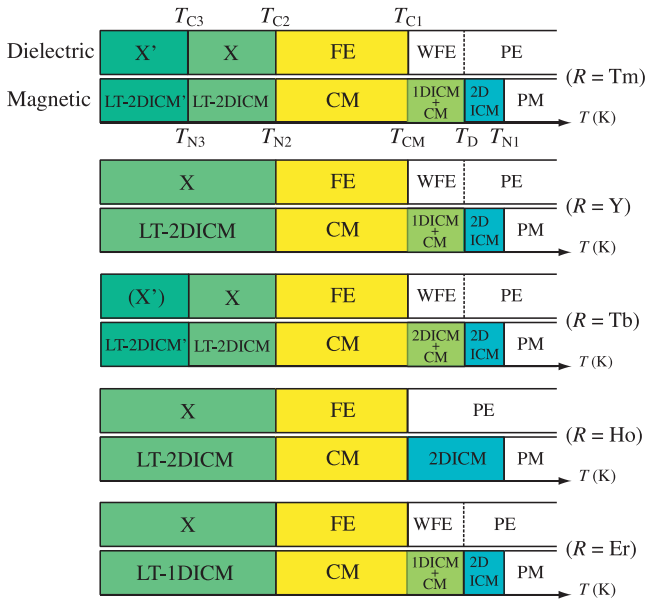

Figure 6. Magnetic and dielectric phase diagram for RMn_2O_5 (R = Tm, Y, Tb, Ho, Er).

It is speculated that the origin of such a peculiar phenomenon is the pinning of magnetic domains. For this reason, it is very difficult to determine the nature of the weak ferroelectric character.

In figure 6, the phase diagrams of RMn_2O_5 (R = Tm, Y, Tb, Ho and Er) are summarized. The figure is slightly modified from the original [55] so as to reflect the newest data. The upper and lower panels for each compound correspond to the dielectric and magnetic phase diagrams, respectively. Higashiyama *et al* introduced a notation (X) for the low temperature phase in their dielectric measurements, because these dielectric phases have not yet been precisely identified [58]. Some of the X and X′ phases have now been clarified, such as the X′ phase of $TmMn_2O_5$, which is a ferroelectric phase along the a-axis below T_{C3}. For the moment, we will refer to the dielectric phases below T_{C2} and T_{C3} as X and X′ phases, respectively, for all five compounds.

4. Colossal magnetoelectric effect and the H–T and P–T phase diagrams

The colossal ME effect observed in RMn_2O_5 has attracted much research, due to the possibilities of new functional materials and new frontiers in applications. In $TbMn_2O_5$, the polarization flip (**P** ∥ **b**) was observed under a relatively low external magnetic field (**H** ∥ **a**), and there was no effect for different directions of the applied magnetic field [12]. A similar effect was found in various RMn_2O_5 compounds [7–11, 13, 58, 59]. Why is such an extraordinary effect observed in this material? To understand this colossal ME effect, an investigation of the magnetic field and temperature phase diagram (H–T phase diagram) for magnetic and dielectric properties is indispensable.

Higashiyama *et al* investigated the dielectric H–T phase diagram of RMn_2O_5 (R = Dy, Ho and Er) [58, 59] as a

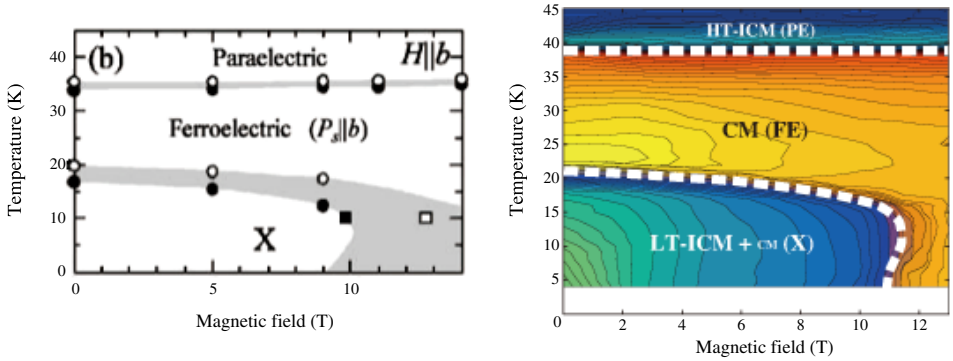

Figure 7. H–T phase diagram of $HoMn_2O_5$. Left: dielectric properties from [58]. Right: magnetic properties from [53]. Magnetic field is expressed as $\mu_0 H$.

response to the magnetic field of three different directions. They found a pronounced effect on **H** ∥ **b** for the dielectric H–T phase diagram of $HoMn_2O_5$, in which the X phase transforms to the ferroelectric phase (**P** ∥ **b**) at low temperature. That is, at low temperature below 20 K, electric polarization is induced by application of a magnetic field. This phenomenon is essentially the same as that for $TbMn_2O_5$, observed by Hur *et al* [12]. There are almost no effects when the magnetic field is along the a- and the c-axes. From this result, the so-called colossal ME effect is simply interpreted as the magnetic-field induced ferroelectric phase transition. Higashiyama *et al* also found that the ferroelectric phase (**P** ∥ **b**) of $ErMn_2O_5$ transforms at low temperature to the X phase under a relatively low magnetic field (**H** ∥ **c**) [58]. Thus, in this case, the ferroelectric phase is suppressed by the magnetic field. In addition, the ferroelectric phase of $ErMn_2O_5$ transforms at low temperature to the X phase under a relatively higher magnetic field (**H** ∥ **a**), but there is no effect on **H** ∥ **b**. As one example, the dielectric H–T phase diagram of $HoMn_2O_5$ on **H** ∥ **b** is shown at the left panel in figure 7.

Next, the corresponding magnetic H–T phase diagram is determined. Low temperature and high magnetic-field neutron experiments were performed on $HoMn_2O_5$. On application of the magnetic field along the b-axis up to $H = 13$ T, the spin structure at the lowest temperature changes markedly. Contour maps of the ICM and CM Bragg intensities were measured around $\mathbf{Q} = (\frac{1}{2}, 0, 2-\frac{1}{4})$ at various temperatures and magnetic fields. At zero field and $T = 4$ K, two peaks are found at the incommensurate position described as the propagation vector of $\mathbf{q}_M \sim (\frac{1}{2} \pm 0.019, 0, \frac{1}{4} + 0.022)$. However, when a magnetic field of 13 T is applied in the field cooling (FC) process, the two incommensurate peaks disappear completely and a single peak appears exactly at the commensurate position. A difference was found between the peak distribution in the FC process and that in the ZFC process, which indicates that there is a large hysteresis at the incommensurate–commensurate phase transition, suggesting a first-order nature of the phase transition.

To observe the correlation between the field response of the microscopic magnetic properties and that of the dielectric properties, the H–T phase diagram was mapped out for the 2DICM, CM, and LT-2DICM phases. The right panel in figure 7 shows a contour map of the intensities of the magnetic signals as functions of temperature and magnetic field, only in the FC process. The boundaries between the phases are approximated by white dashed lines. Distributions for each phase are expressed by a gradation sequence. The phase diagram obtained clearly shows that 2DICM is completely field independent, whereas the LT-2DICM phase rapidly disappears and the CM phase forms around $H \sim 11$ T. Interestingly, a comparison of our H–T phase diagram with the dielectric phase diagram reveals that the LT-2DICM and CM phases correspond exactly to the weak ferroelectric (X) phase and the robust ferroelectric (FE) phase, respectively. The one-to-one correspondence between the magnetic and dielectric properties clearly shows that the FE phase is magnetically induced. These experimental observations clearly establish that the commensurate spin state is indispensable for magnetic field-induced ferroelectricity. Thus, the dielectric properties in this system have a magnetic origin.

Similar neutron experiments were performed for $ErMn_2O_5$ on application of a magnetic field along the c-axis [60]. Again, a one-to-one correspondence between the magnetic and dielectric phase diagram was obtained. That is, the magnetic properties on the H–T phase diagram correspond exactly to the dielectric properties.

Very recently, a new discovery was reported on the pressure–temperature (P–T) phase diagram of RMn_2O_5 by Cruz *et al* [61] and by Jo *et al* [62]. They observed the dielectric properties of RMn_2O_5 (R = Tb, Dy and Ho) as functions of hydrostatic pressure and temperature, shown on the left of figure 8. Surprisingly, the P–T and H–T phase diagrams closely resemble one another, or are almost identical when the magnetic and pressure axes are normalized. Neutron experiments were then performed to study the magnetic properties in the P–T phase diagram of $HoMn_2O_5$ [63], and exactly the same relation as for the H–T phase diagram in figure 7 was found, as shown in the right of figure 8. At the moment, we have no information as to how the magnetic field and pressure influence the magnetic interaction. However, this line of study might be one of the experimental keys to understanding the origin of magnetically induced ferroelectricity in RMn_2O_5.

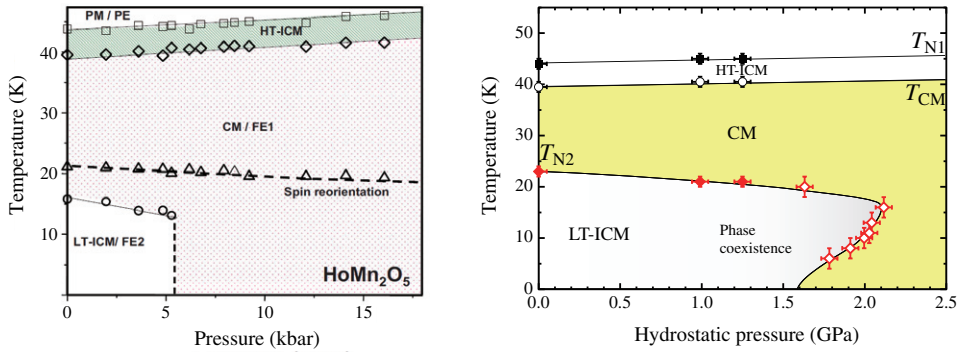

Figure 8. P–T phase diagram of $HoMn_2O_5$. Left: dielectric properties from [61]. Right: magnetic properties from [63].

5. Magnetic structure

Concerning the magnetic structure analysis of RMn_2O_5, many neutron powder experiments have been conducted. Usually, a waveform is assumed for describing the magnetic moments to solve the magnetic structure, especially in the case of an incommensurate phase. For the analysis, the number of waves that are included is crucial to reach a proper result. For the commensurate phase, it is possible to solve the magnetic structure without any model in principle. In reality, however, for the RMn_2O_5 system, it is very difficult to use this method, because there are many fitting parameters. If we consider a $2a_0 \times b_0 \times 4c_0$ magnetic unit cell, where $a_0 \times b_0 \times c_0$ is the chemical unit cell of the prototype phase, then 32 molecules are included ($Z = 32$). Thus, $32R^{3+}$, $32Mn^{3+}$ and $32Mn^{4+}$ magnetically active ions are included. Therefore, the number of unknown magnetic parameters is 288, and for such a complicated magnetic structure it is almost impossible to solve using neutron powder diffraction data. Thus, usually, a model described by the magnetic moment waveform is used to solve the magnetic structure. As described later, a magnetic extinction rule was identified; thus, the number of independent magnetic moments is reduced to 72 if R^{3+} ions are magnetically active, and to 48 for YMn_2O_5. Even with this number, it is difficult to solve the structure using neutron powder diffraction data. Therefore, we would like to emphasize the advantage of single crystal neutron experiments, because each Bragg reflection is separately observed, and there is no ambiguity in the indexing and accumulation of the intensity data.

Intensity data measurements of various RMn_2O_5 single crystals were performed using a FONDER. The magnetic diffraction intensity was measured up to $2\theta_{max} = 73°$, and the nuclear Bragg intensity was measured up to $2\theta_{max} = 156°$, using a $2a_0 \times b_0 \times 4c_0$ unit cell. Systematic absences of magnetic Bragg reflections were found in the $2a_0 \times b_0 \times 4c_0$ unit cell. The allowed magnetic Bragg reflections are indexed as (hkl), where $h = 2n + 1$ and $l = 2m + 1$. Two magnetic symmetry operations, $\mathbf{m}(\mathbf{r} + \mathbf{a}_0) = -\mathbf{m}(\mathbf{r})$ and $\mathbf{m}(\mathbf{r} + 2\mathbf{c}_0) = -\mathbf{m}(\mathbf{r})$, are introduced. The real magnetic unit cell must be $\mathbf{a}_M = \mathbf{a}_0 - 2\mathbf{c}_0$, $\mathbf{b}_M = \mathbf{b}_0$ and $\mathbf{c}_M = \mathbf{a}_0 + 2\mathbf{c}_0$. The independent magnetic moment components are then 72 for $8R^{3+}$, $8Mn^{4+}$ and $8Mn^{3+}$ atoms, and if R^{3+} ions are non-magnetic such as for

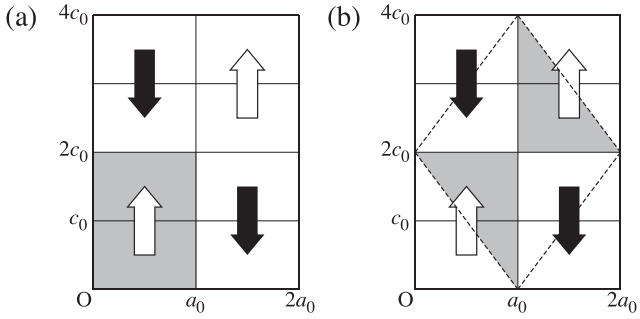

Figure 9. Magnetic unit cell. The figure is taken from [32].

YMn_2O_5, they are reduced to 48. Figure 9 shows the magnetic unit cell. On the left-hand side, the $2a_0 \times b_0 \times 4c_0$ magnetic unit cell is shown with the magnetic moment pattern based on the requirement of the magnetic extinction rule. On the right-hand side, the actual magnetic unit cell is shown with a dotted line.

It is well known that the results of structure analyses for complicated structures strongly depend on the initial assumptions of the structural model, especially when data are derived from neutron powder diffraction. Thus, in the present study, we have performed a model-free analysis of the magnetic structures in the commensurate magnetic phase, i.e., the ferroelectric phase, for the RMn_2O_5 system using single crystal neutron diffraction. The magnetic structure analyses of RMn_2O_5 (R = Y, Er, Ho, and Tm) have been completed [31, 32, 64]. Following is a brief explanation of how the magnetic structures were obtained. First, an ordinal crystal structure analysis is conducted using nuclear Bragg reflections. Thus, the scale factor and the extinction parameter are obtained, as well as the crystal structure parameters. Once the scale factor is obtained, the magnetic intensity is straightforwardly converted to magnetic structure factors. A Monte Carlo simulation technique is applied to obtain initial estimates of the magnetic structure. If the reliability factor (R-factor) is reasonably low, then a random walk process around the given parameter set is started to obtain better initial estimates. After this, the conventional least squares fitting procedure is applied to refine the magnetic moment parameters. Actually speaking, all of the obtained initial estimates obtained by a Monte Carlo simulation converted to

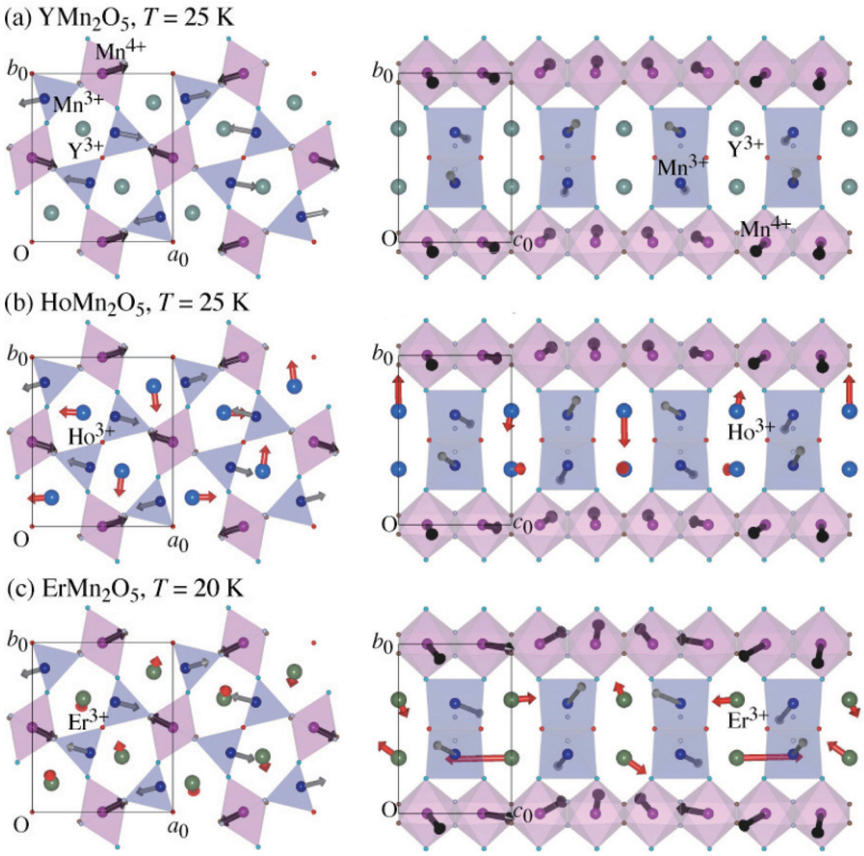

Figure 10. Magnetic structure of RMn_2O_5 (R = Y, Er and Ho) projected on the *ab*- and *bc*-planes [32].

the same answer. That is, we consider that the least squares fitting procedure reaches the absolute minimum of χ^2 in the parameter space.

The detailed analysis of YMn_2O_5 at 25 K is described here as an example. First, the crystal structure analysis results were $a = 7.263(3), b = 8.476(2), c = 5.660(1)$ Å, $Z = 4$, $Pbam$, $\lambda = 1.24$ Å, $2\theta_{max} = 120°$, data number = 419, $R(F) = 0.033$. The magnetic diffraction intensity was then measured up to $2\theta_{max} = 73°$ using the $2a_0 \times b_0 \times 4c_0$ unit cell. Using the obtained scale factor of the crystal structure analysis, the magnetic structure factors are scaled so that an additional scale factor is not required for the magnetic structure analysis. The total data number used for the magnetic structure analysis was 139, and the reliability factor for the model-free analysis was $R(F) = 0.066$. Detailed magnetic moments obtained by the least squares fitting procedures for R = Y, Er and Ho are tabulated in references [31, 32]. The spin configuration on the *ab*- and *bc*-planes is shown in figure 10. The spin structure of Mn^{4+} and Mn^{3+} is essentially the same for R = Y, Er, Ho and Tm. The moment of R^{3+} is also shown in the figure, and the difference in the spin parameter can be seen by the direction of the R^{3+} moments. The major direction of R^{3+} ion moments is along the *a*- and the *b*-axes for Ho^{3+}, and the *c*-axis for Er^{3+}, as shown in figure 10. These moments of rare earth ions are not spontaneous, but might be induced by the local magnetic field of Mn ions.

It was also demonstrated that the obtained magnetic moment component shows a cosine wave along the *c*-axis; that is, the magnetic moments (M_x, M_y, M_z) are shown as a function of z for Mn^{4+} octahedron and Mn^{3+} pyramid chains [31, 32]. We have also shown that the obtained phases of the cosine wave for each chain are simply $0, \pi$ and $\pm\pi/2$ within the experimental error. This result naturally suggests that the spin configuration of Mn^{3+} and Mn^{4+} ions is a transverse spiral propagating along the *c*-axis. Our experimental results demonstrate that the spin configuration of Mn^{3+} and Mn^{4+} ions in the CM phase is essentially common to YMn_2O_5, $ErMn_2O_5$ and $HoMn_2O_5$, regardless of the type of R^{3+} ion, whose magnetic structure is a transverse spiral propagating along the *c*-axis. These results are in sharp contrast to those obtained by powder neutron magnetic structure analyses [25–27, 41], because the assumed model does not include the *c*-component.

6. Lattice modulation

As a lattice response for magnetic ordering of RMn_2O_5, Higashiyama *et al* first found a superlattice reflection at $\mathbf{Q} = (0, 0, 4.5)$ in the reciprocal lattice space of $DyMn_2O_5$ in the FE and CM phase using SR [59]. This position corresponds to double the magnetic modulation vector $\mathbf{q}_M$. However, because they had no information on $\mathbf{q}_M$ as a function of temperature, no report of the superlattice reflections in the ICM phase was made. We performed precise measurements for the superlattice reflections of RMn_2O_5 (R = Y, Tb) in all of

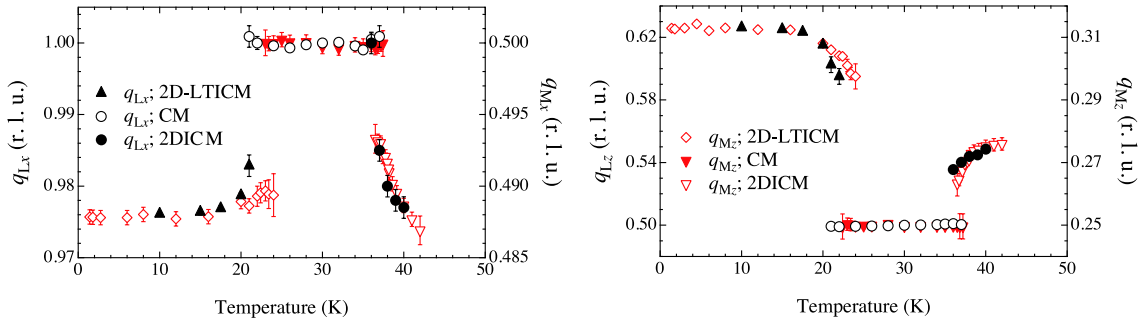

Figure 11. **q**-vectors of lattice modulation and magnetic propagation vectors of $TbMn_2O_5$. The q_z-component (right) is added to the q_x-data (left) given in [65].

the phases, 2DICM, CM and LT-2DICM, using SR [31, 65]. It was found that the lattice modulation vector $\mathbf{q}_L$ is exactly double that of the magnetic propagation vector $\mathbf{q}_M$ in all of the phases: $\mathbf{q}_L = 2\mathbf{q}_M$. Very recently, Koo *et al* reported similar experiments for superlattice reflections of $TbMn_2O_5$ [66], and the result was essentially the same. Our experimental details are given in [65]. First, the presence of superlattice reflections was surveyed using SR at PF-BL4C. In the next step, a structure analysis of the commensurate phase of $TbMn_2O_5$ was attempted. An attempt was made to use a conventional imaging-plate system at PF-BL1B, but this was unsuccessful, because the intensity of the superlattice reflection was too weak, and the signal-to-background (S/N) ratio was approximately one. When the conventional photographic technique was applied with rotation of the crystal, only the background was accumulated, and the S/N ratio dropped significantly, so that the final S/N ratio was approximately 1/500. Intensity data were then acquired at PF-BL4C, using a scintillation counter, for a preliminary structure analysis of the atomic displacement pattern. The measurement temperature was 30 K.

Very weak superlattice reflections were found at $\mathbf{q}_L = (2\delta_x, 0, \frac{1}{2} + 2\delta_z)$ below T_N around the fundamental Bragg reflection indexed with $h = 2n + 1$. The ratio between the fundamental and the superlattice reflection was approximately 10^{-6}. The lattice modulation wavevector $\mathbf{q}_L$ was exactly twice that of the magnetic propagation vector $\mathbf{q}_M$, as mentioned above, $\mathbf{q}_L = 2\mathbf{q}_M$. There was no intensity around $h = 2n$, and this appeared to be indicative of an extinction rule.

On cooling, the $\mathbf{q}_L$-vector moved toward the commensurate position, and the intensity gradually increased. At T_{C1}, the position of the superlattice reflection suddenly moved to another reciprocal position, indexed by $h = 2n$, and the original superlattice reflection around $h = 2n+1$ disappeared. The lattice modulation wavevector $\mathbf{q}_L$ was commensurate and could be expressed by $\mathbf{q}_L = (0, 0, \frac{1}{2})$. Again, this position is exactly twice the magnetic propagation vector $\mathbf{q}_M$. The ratio between the fundamental and the superlattice reflection in the commensurate ferroelectric phase reached approximately 10^{-5}.

On further cooling and crossing T_{C2}, the position of the superlattice reflection again suddenly became incommensurate around the fundamental Bragg reflection indexed by $h = 2n + 1$. The $\mathbf{q}_L$ vector of $TbMn_2O_5$, observed using x-rays, is shown in figure 11, and is associated with the $\mathbf{q}_M$ vector observed using neutrons [54]. Note that the vertical axes for the $\mathbf{q}_M$ and the $\mathbf{q}_L$ vectors are different from each other by a factor of two. The $\mathbf{q}_L$-vector of YMn_2O_5 was also measured as a function of temperature, and again the result was the same.

The lattice modulation corresponds to the magnetostriction waves. A trial to solve such an atomic displacement pattern was reported for $TbMn_2O_5$ [31, 65] and YMn_2O_5 [67], based on the space group $Pb2_1m$ ($Z = 8$). The space group $Pb2_1m$ ($Z = 4$) was first proposed by Kagomiya *et al* [68], and later Blake *et al* discussed the magnetic symmetry in connection with the crystal space group $Pb2_1m$ ($Z = 4$) in their neutron powder experiments [26]. The present space group, $Pb2_1m$ ($Z = 8$), seems to be similar to the previously proposed one, but the distributions of symmetry elements are essentially different from each other, because the unit cell size is different. Evidence for the crystal symmetry as the space group $Pb2_1m$ ($Z = 8$) was investigated for YMn_2O_5 [67] using the SR at SPring-8 BL02B1. The extinction rule was confirmed and new superlattice reflections corresponding to the polar displacements were found. For the crystal structure analysis in the FE phase, 180 superlattice reflection data at $\mathbf{q}_L$ and six reflections corresponding to the $\mathbf{q} = 0$ position were used. The magnetostriction pattern is successfully solved, but the homogeneous displacement pattern including the polar displacement cannot be solved uniquely, because the data points are still less than the fitting parameters. The detailed data will be published elsewhere. Very recently, Koo *et al* published the same results for $TbMn_2O_5$ [66] using resonant SR experiments. Even though their findings were limited to only $\mathbf{Q} = (3, 0, 0)$, this is clear evidence of the existence of a $\mathbf{q} = 0$ type displacement order parameter in this system. It should be mentioned that this index does not reflect the polar displacements in the FE phase, because the displacements relating to electric polarization are along the b-axis. Rather, this Bragg reflection is an observation of the breaking of the a-glide mirror plane relating to the internal displacement pattern (so-called TO mode condensation) in the unit cell.

7. Discussion

As described in the previous sections, the so-called colossal magnetoelectric effect (CME) in RMn_2O_5 is interpreted as phase transition phenomena induced by an external

magnetic field. The same effect is also seen by application of hydrostatic pressure. This effect reminds us of the colossal magnetoresistance (CMR) effect [69]. The CMR effect is based on the coupling between conduction electrons and spin state on the electronic levels or orbital. The phase transition from the paramagnetic phase to the ferromagnetic phase changes the transfer integral probability due to the relevant interaction properties in this system. Depending on the type of the magnetic ordered phase, electron transport properties drastically change. That is, the phase transition is the key concept for the colossal effect. In the case of CME, again the phase transition is the key concept. The ordinal ME effect is very small, but the recent topics of CME are not the ordinal phenomena. If we believe the chirality-induced polarization model, the spin pattern induces spontaneous polarization, and the change of the spin pattern changes the spontaneous polarization dramatically. This gives the CME, and the phase transition is indispensable to understand this phenomenon. The only difference of CME and CMR is that the former is the phase transition between the ordered phases while the latter is the phase transition from the disordered phase to the ordered phase. The situation of CME seen in $RMnO_3$ perovskite type compounds is completely the same.

The robust CM and FE phases of RMn_2O_5 might be responsible for Mn^{3+} and Mn^{4+} moments. The transition to the LT-2DICM phase at T_{C2} is observed for all of the common family compounds, even in YMn_2O_5. Thus, the origin of the CM and FE phases, as well as the cause of diminishment in the CM and FE phases, might be common, based on the frustration of Mn^{3+} and Mn^{4+} interactions. On the other hand, a variety of phases and physical properties, especially as a response to the external field, are introduced by the 4f moment of the rare earth R^{3+} ions in the weak FE phase, or so-called X phase, below T_{C2}. Although the details are still unclear, the complicated behavior with the applied magnetic field might indicate a field response related to the R^{3+} moment induced by the ordering of Mn^{3+} and Mn^{4+} moments. The magnetic structure analysis under zero field using a single crystal shows that Ho^{3+} moments of up to $\sim$1.3 μ_B and Er^{3+} moments of up to $\sim$3.2 μ_B are induced, even above 20 K (CM phase). As shown in figure 10, the difference in the spin parameter can be seen by the direction of the R^{3+} moments. The major direction of R^{3+} ion moments is along the a- and the b-axes for Ho^{3+}, and the c-axis for Er^{3+}.

Our results have shown that the magnetic field strongly affects the magnetism below $\sim$20 K (T_{C2} at zero field), whereas the magnetism above $\sim$20 K is almost field independent. This strongly suggests that the 4f moment of rare earth atoms, whose amplitude increases with decreasing temperature, contributes significantly to the field responses of the magnetic and dielectric properties in the weak FE or X phase. From the numerous studies that have been conducted, a large ME effect has only been observed in the lower temperature region below T_{C2} [12, 13, 58]. Recent systematic analyses of the magnetic structure of RMn_2O_5 (R = Y, Er, Ho, Tb, and Dy) have shown that the magnetic interaction in the Mn^{3+} and Mn^{4+} sublattices is geometrically frustrated [25, 26, 31, 32, 41, 64]. Such magnetic frustration might induce a competing magnetic ground state that can be easily tuned by the f–d spin exchange interaction between the R^{3+} and $Mn^{3+,4+}$ ions.

An interesting issue is the direction of the 4f moment as mentioned above. There is a strong correlation between the direction of the 4f moment and the applied magnetic field in which a major response occurs. Er^{3+} moments are aligned along the c-axis, while Ho^{3+} moments are along the a- and b-axes in the CM phase, as denoted above [26, 32]. These axes are the easy axes for each of the rare earth elements. As shown by Higashiyama [58], a major response is observed in the H–T phase diagram when the direction of the magnetic field is the c-axis for R = Er and the b-axis for R = Ho. The same relation is seen in R = Tb, that is, the direction of the 4f moment is along the a-axis while the major response is observed again on the magnetic field along the a-axis [12, 26]. The only exception is R = Dy; the 4f moment along the b-axis and the magnetic field along the a-axis [13, 26, 59]. A response to the magnetic field from non-magnetic R = Y compounds is not observed at lower magnetic fields. However, as reported by Popov *et al*, when a high magnetic field above 200 kOe (ca 20 T) is applied, the FE phase with $P \parallel b$ is induced by $H \parallel b$, and $P \parallel a$ is induced by $H \parallel a$ [11].

In this paper, we have discussed the family compounds with relatively small ionic radius rare earth elements (R = Tb, Ho,Er, Tm and Y), because RMn_2O_5 with larger ionic radius rare earth elements have slightly different magnetic character. For instance, R = Eu shows a $q_z = 1/3$ CM phase [70], and R = Bi shows a $q_z = 1/2$ CM phase [71]. The global scheme of this system is highly interesting and should be investigated in future work.

Based on the model-free magnetic structure analysis using a single crystal, it was concluded that the transversal spiral spin structure is indispensable to consider the origin of the electric polarization. By combining the theory [35] and the elucidated magnetic structure [31, 32, 35], the electric dipole moment can be analytically obtained for two chains (A chain and B chain) of Mn^{4+}. The result is $P_{Ax} = -P_{Bx} = \Delta z M_{x0} M_{y0} \sin(\pi \Delta z/2)$, $P_{Ay} = P_{By} = \Delta z M_{y0} M_{z0} \sin(\pi \Delta z/2)$ and $P_{Az} = P_{Bz} = 0$. Here, Δz is the distance between neighboring Mn^{4+} atoms (0.49 and 0.51 depending on z), and M_{x0}, M_{y0} and M_{z0} are the x, y and z-component amplitudes of the moment, respectively. The amplitudes in the A chain and B chain are not equivalent in our treatment, but they are very close to each other. In our analysis, only two magnetic symmetry operations were used, that correspond to the magnetic extinction rules. If we introduce the proper magnetic space group, these two chains might be equivalent from the symmetry. Conversely, the proper magnetic space group and symmetries can be determined from our precise data [72].

If we consider the four Mn^{3+} chains (C, D, E and F chains), which is rather indirect coupling, we obtain similar relations: $P_{Cx} = -P_{Dx} = -P_{Ex} = P_{Fx}$, $P_{Cy} = P_{Dy} = P_{Ey} = P_{Fy}$ and $P_{Cz} = P_{Dz} = P_{Ez} = P_{Fz} = 0$. This scenario is attractive, since the ferroelectric character along the b-axis is naturally explained with a very simple model. However, there are several difficulties in this model when considering the experimental evidence reported so far: (1) antiferroelectric

character exists along the a-axis, because the major moment is the a-component, (2) a ferrielectric character exists along the b-axis, (3) the c-direction displacement experimentally observed by SR is not created in this model and (4) the meaning of the lock-in transition of q_z-modulation at T_D is unclear, since the theory works regardless of commensurability. However, the recent discovery of the polarization flop transition from the b-axis to the a-axis in $TmMn_2O_5$ indicates the importance of the a-component polarization [52]. Furthermore, ferrielectric character is observed in $ErMn_2O_5$ as shown in figure 5 [57]. Thus, some of the difficulties in this scenario have already been removed.

The spin modulation along the a-axis is rather complicated. The interaction path is a three dimensional zig-zag chain: Mn^{4+}–O–Mn^{3+}–O–Mn^{3+}–O–Mn^{4+}. Already Chapon *et al* have evaluated the antiferromagnetic interaction energy and pointed out the importance of this plane in $TbMn_2O_5$ in terms of inducing polarization [25]. For this scenario, a well defined spin configuration on the ab-plane is required, and lock-in of the q_z-direction gives such a condition, regardless of incommensurability along the q_x-direction at T_D. Of course, we will not ignore the possibility of the combination of two scenarios, in which the exchange striction mechanism works only in the CM phase, added to the spin chirality mechanism in the ICM phases (see figure 3 of [56]). To distinguish the two scenarios, it is indispensable to solve the magnetic structure of both the LT-2DICM and LT-1DICM phases. In addition, a precise atomic displacement pattern for the FE phase is required, and such work is planned for the near future.

Acknowledgments

We thank Drs Wakimoto, Kakurai and Metoki of the Japan Atomic Energy Agency for performing the neutron diffraction experiments under high magnetic field. We also thank Drs Aso, Uwatoko and their co-workers at the Institute for Solid State Physics for performing neutron diffraction experiments under high pressure. This work was supported by the Yamada Science Foundation, a Grant-in-Aid for Scientific Research (B) No 16340096, a grant in Priority Areas No 19052001 from the Ministry of Education, Culture, Sports, Science and Technology, Japan, and the Interuniversity Cooperative Research Program, No 30, of the Institute for Materials Research, Tohoku University.

References

[1] Aizu K 1970 *Phys. Rev.* B **2** 754
[2] Smolenskii G A and Bokov V A 1964 *J. Appl. Phys.* **35** 915
[3] Smolenskii G A, Yudin V M, Sher E S and Stolypin Yu E 1963 *Sov. Phys.—JETP* **16** 622
[4] Fiebig M 2005 *J. Phys. D: Appl. Phys.* **38** R123
[5] Kimura T, Goto T, Shintani H, Ishizaka K, Arima T and Tokura Y 2003 *Nature* **426** 55
[6] Iwata N and Kohn K 1998 *Ferroelectrics* **219** 161
[7] Koyata Y, Nakamura H, Iwata N, Inomata A and Kohn K 1996 *J. Phys. Soc. Japan* **65** 1383
[8] Koyata Y and Kohn K 1997 *Ferroelectrics* **204** 115
[9] Iwata N, Uga M and Kohn K 1997 *Ferroelectrics* **204** 97
[10] Uga M, Iwata N and Kohn K 1998 *Ferroelectrics* **219** 55
[11] Popov Yu F, Kadomtseva A M, Krotov S S, Vorob'ev G P, Kamilov K I, Lukina M M and Tegranchi M M 2003 *J. Exp. Theor. Phys.* **96** 961
[12] Hur H, Park S, Sharma P A, Ahn J, Guha S and Cheong S-W 2004 *Nature* **429** 392
[13] Hur N, Park S, Sharma P A, Guha S and Cheong S-W 2004 *Phys. Rev. Lett.* **93** 107207
[14] Sanina V A, Sapozhnikova L M, Golovenchits E I and Morozov N V 1988 *Sov. Phys.—Solid State* **30** 1736
[15] Golovenchits E I, Morozov N V, Sanina V A and Sapozhnikova L M 1992 *Sov. Phys.—Solid State* **34** 56
[16] Kohn K 1994 *Ferroelectrics* **162** 1
[17] Ikeda A and Kohn K 1995 *Ferroelectrics* **169** 75
[18] Inomata A and Kohn K 1996 *J. Phys.: Condens. Matter* **8** 2673
[19] Kagomiya I and Kohn K 1998 *Ferroelectrics* **219** 169
[20] Fujita T and Kohn K 1998 *Ferroelectrics* **219** 155
[21] Kohn K and Kagomiya I 1999 As a review of RMn_2O_5 family *J. Cryst. Soc. Japan* **41** 342 (in Japanese)
[22] Bertaut E F, Buisson G, Durif A, Mareshal J, Montmory M C and Quezel-Ambrunaz S 1965 *Bull. Soc. Chim. Fr.* **1132**
[23] Abrahams S C and Bernstein J L 1967 *J. Chem. Phys.* **46** 3776
[24] Alonso J A, Casais M T, Martínez-Lope M J, Martínez J L and Fernández-Díaz M T 1997 *J. Phys.: Condens. Matter* **9** 8515
[25] Chapon L C, Blake G R, Gutmann M J, Park S, Hur N, Radaelli P G and Cheong S-W 2004 *Phys. Rev. Lett.* **93** 177402
[26] Blake G R, Chapon L C, Radaelli P G, Park S, Hur N, Cheong S-W and Rodríguez-Carvajal J 2005 *Phys. Rev.* B **71** 214402
[27] Buisson G 1983 *Phys. Status. Solidi.* a **16** 533 (in French)
[28] Buisson G 1983 *Phys. Status. Solidi.* a **17** 191 (in French)
[29] Wilkinson C, Sinclair F, Gardner P, Forsyth J B and Wanklyn B M R 1981 *J. Phys. C: Solid State Phys.* **14** 1671
[30] Gardner P, Wilkinson C, Forsyth J B and Wanklyn B M R 1988 *J. Phys. C: Solid State Phys.* **21** 5653
[31] Noda Y, Kimura H, Kamada Y, Osawa T, Fukuda Y, Ishikawa Y, Kobayashi S, Wakabayashi Y, Sawa H, Ikeda N and Kohn K 2006 *Physica* B **385/386** 119
[32] Kimura H, Kobayashi S, Fukuda Y, Osawa T, Kamada Y, Noda Y, Kagomiya I and Kohn K 2007 *J. Phys. Soc. Japan* **76** 074706
[33] Kagomiya I, Kimura H, Noda Y and Kohn K 2001 *ASR-2000: Proc. 1st Int. Symp. Advanced Science Research 'Advances in Neutron Scattering Research'*; *J. Phys. Soc. Japan* **70** (Suppl. A) 145
[34] Noda Y, Fukuda Y, Kimura H, Kagomiya I, Matsumoto S, Kohn K, Shobu T and Ikeda N 2003 *Proc. 4th Japan–Korea Conf. on Ferroelectricity (JKC-FE2002)*; *J. Korean Phys. Soc.* **42** S1192
[35] Katsura H, Nagaosa N and Balatsky A V 2005 *Phys. Rev. Lett.* **95** 057205
[36] Sergienko I A and Dagotto E 2006 *Phys. Rev.* B **73** 094434
[37] Dzyaloshinskii I 1958 *J. Phys. Chem. Solids* **4** 241
[38] Moriya T 1960 *Phys. Rev.* **120** 91
[39] Goodenough J B 1955 *Phys. Rev.* **100** 564
[40] Kanamori J 1959 *J. Phys. Chem. Solids* **10** 87
[41] Chapon L C, Radaelli P G, Blake G R, Park S and Cheong S-W 2006 *Phys. Rev. Lett.* **96** 097601
[42] Wanklyn B 1972 *J. Mater. Sci.* **7** 813
[43] Noda Y, Kimura H, Kiyanagi R, Kojima A, Morii Y, Minakawa N and Takesue N 2001 *(ASR-2000): Proc. 1st Int. Symp. Advanced Science Research 'Advances in Neutron Scattering Research'*; *J. Phys. Soc. Japan* **70** (Suppl. A) 456
[44] Valasek J 1921 *Phys. Rev.* **17** 475

[45] Mitsui T 1958 *Phys. Rev.* **111** 1259
[46] Sawada A 1991 *J. Phys. Soc. Japan* **60** 3593
[47] Hashiguchi I, Kuroiwa Y and Sawada A 1999 *J. Phys. Soc. Japan* **68** 2673
[48] Kobayashi S, Osawa T, Kimura H, Noda Y, Kagomiya I and Kohn K 2004 *J. Phys. Soc. Japan* **73** 1593
[49] Kobayashi S, Osawa T, Kimura H, Noda Y, Kagomiya I and Kohn K 2004 *J. Phys. Soc. Japan* **73** 1031
[50] Fukunaga M, Nishihata K, Kimura H, Noda Y and Kohn K 2007 *J. Phys. Soc. Japan* **76** 074710
[51] Kobayashi S, Kimura H, Noda Y and Kohn K 2005 *J. Phys. Soc. Japan* **74** 468
[52] Fukunaga M, Nishihata K, Kimura H, Noda Y and Kohn K 2008 *J. Phys. Soc. Japan* **77** at press
[53] Kimura H, Kamada Y, Noda Y, Kaneko K, Metoki N and Kohn K 2006 *J. Phys. Soc. Japan* **75** 113701
[54] Kobayashi S, Osawa T, Kimura H, Noda Y, Kasahara N, Mitsuda S and Kohn K 2004 *J. Phys. Soc. Japan* **73** 3439
[55] Kobayashi S, Osawa T, Kimura H, Noda Y, Kagomiya I and Kohn K 2005 *J. Korean Phys. Soc.* **46** 289
[56] Fukunaga M, Kimura H, Noda Y and Kohn K 2007 *J. Korean Phys. Soc.* **51** 768
[57] Fukunaga M and Noda Y 2008 *J. Phys. Soc. Japan* **77** 064706
[58] Higashiyama D, Miyasaka S and Tokura Y 2005 *Phys. Rev.* B **72** 064421
[59] Higashiyama D, Miyasaka S, Arima T and Tokura Y 2004 *Phys. Rev.* B **70** 174405
[60] Kimura H *et al* 2007 unpublished data
[61] dela Cruz C R, Lorenz B, Sun Y Y, Wang Y, Park S, Cheong S-W, Gospodinov M M and Chu C W 2007 *Phys. Rev.* B **76** 174106
[62] Jo Y, Jang K-H, Park J-G, Kim H C, Kim T H, Kim K H, Hur N, Park S and Cheong S-W 2007 *Phys. Rev.* B **76** 012406
[63] Kimura H, Nishihata K, Noda Y, Aso N, Matsubayashi K, Uwatoko Y and Fujiwara T 2008 *J. Phys. Soc. Japan* **77** 063704
[64] Kimura H *et al* 2007 unpublished data
[65] Noda Y, Kimura H, Kamada Y, Ishikawa Y, Kobayashi S, Wakabayashi Y, Ikeda N and Kohn K 2007 *J. Korean Phys. Soc.* **51** 828
[66] Koo J, Song C, Ji S, Lee J-S, Park J, Jang T-H, Yang C-H, Park J-H, Jeong Y H, Lee K-B, Koo T Y, Park Y J, Kim J-Y, Wermeille D, Goldman A I, Srajer G, Park S and Cheong S-W 2007 *Phys. Rev. Lett.* **99** 197601
[67] Noda Y *et al* 2007 unpublished data
Noda Y 2007 *Annual Mtg of Japanese Synchrotron Radiation Society (Hiroshima, Jan. 2007)* (Abstract, p.53)
Kamda Y 2006 *Master Thesis* Tohoku University (in Japanese)
Nishihata K 2008 *Master Thesis* Tohoku University (in Japanese)
[68] Kagomiya I, Matsumoto S, Kohn K, Fukuda Y, Shobu T, Kimura H, Noda Y and Ikeda N 2003 *Ferroelectrics* **286** 889
[69] Tokura Y 2006 *Rep. Prog. Phys.* **69** 797
[70] Polyakov V, Plakhty V, Bonnet M, Burlet P, Regnault L-P, Gavrilov S, Zobkalo I and Smirnov O 2001 *Physica* B **297** 208
[71] Munoz A, Alonso J A, Casais M T, Martinez-Lope M J and Martinez J L 2002 *Phys. Rev.* B **65** 144423
[72] Harris B 2008 private communication